Applied Catalysis B: Environmental 342 (2024) 123329

Contents lists available at ScienceDirect

Applied Catalysis B: Environmental

journal homepage: www.elsevier.com/locate/apcatb

Spectroscopic determination of metal redox and segregation effects during CO and CO/NO oxidation over silica-supported Pd and PdCu catalysts

Stephen Kristy [a,b], Scott Svadlenak [a], Adam S. Hoffman [b], Simon R. Bare [b], Konstantinos A. Goulas [a,*]

[a] School of Chemical, Biological and Environmental Engineering, Oregon State University, Corvallis, OR 97331, USA
[b] Stanford Synchrotron Radiation Lightsource, SLAC National Accelerator Laboratory, Menlo Park, CA 94025, USA

ARTICLE INFO

Keywords:
Diesel Oxidation Catalysis
PdCu alloy
Operando X-ray absorption spectroscopy
Operando infrared spectroscopy

ABSTRACT

We report the effects of alloying Cu into silica supported Pd nanoparticles on the catalytic activity, surface composition, and particle structure during CO oxidation Pd is highly active for CO oxidation but is inhibited by relevant competitive reagents (e.g. NO) at low temperatures (< 150 °C). By alloying Cu into Pd nanoparticles, NO inhibition is suppressed without any CO oxidation activity loss. Infrared spectroscopy illustrates the formation of surface nitrosyl (NO-Pd) is eliminated in the PdCu alloy catalyst, preventing CO oxidation inhibition by NO. X-ray absorption spectroscopy studies show that Pd in the monometallic catalyst forms a surface oxide after light-off. Conversely, in the PdCu catalyst, Pd remains metallic during reaction, independent of temperature, whereas the Cu oxidizes when the catalyst becomes active, after light-off. Furthermore, DRIFTS studies show that the Cu segregates to the surface as the catalyst becomes active for diesel oxidation, presumably becoming the O_2 adsorption site.

1. Introduction

Diesel engines are common in vehicles and equipment throughout the world due to the high efficiency, durability, and widespread infrastructure [1]. The aftertreatment on diesel exhaust systems typically comprises of a series of unit operations, including catalytic reactors, particulate traps and adsorption systems [2] to convert harmful species to inert species. These technologies exist because untreated diesel emissions are carcinogenic and contribute to respiratory health problems. [3,4] The first catalytic reactor in the train of operations is the Diesel Oxidation Catalyst (DOC), which oxidizes CO and hydrocarbons to CO_2 and a portion of NO to NO_2.

Traditionally, DOCs are composed of PtPd alloys on alumina support wash coated onto ceramic monoliths. [5,6] These catalysts are highly effective at high temperatures (330 °C – standard diesel operating temperature) and low CO concentrations, representative of traditional diesel exhaust. [7,8] At high operating temperatures, the thermodynamic equilibrium drives the adsorbates off the surface, resulting in complete oxidation of CO and hydrocarbons, as well as equilibrium conversion of NO to NO_2. However, at low temperatures, such as during engine startup, PtPd surfaces can be blocked or poisoned by CO, preventing O_2 activation. [6,9] Several investigators also demonstrate that increasing the CO fraction in exhaust also leads to a decrease in PtPd DOC effectiveness, [5,10] due to the CO strongly binding to the surface and blocking active sites. [11]. Furthermore, the presence of competitive reagents such as NO or hydrocarbons are shown to compound the effects of poisoning and decrease effectiveness of PtPd DOCs. [9] Modern low-temperature combustion (LTC) diesel vehicles achieve high fuel efficiencies and lower NO_x emissions, compared to conventional diesel vehicles, at the price of higher CO emissions. [7] This is due to low exhaust temperatures and high CO gas concentrations (~0.5 vol% CO) in exhaust, limiting the effectiveness of DOCs. [7,12] Therefore, there is a need to design DOCs that operate effectively at low temperatures and high CO concentrations in the presence of competitive adsorbates.

Different approaches have been taken towards improving DOC activity at low temperature. Zeolite supports have been used in place of alumina to promote oxidation reactions over Pt and Pd. [13–15] Another promising methodology is the use of bimetallic alloys. Franken et al. proposed the use of PtMn as a diesel oxidation catalyst. [16] To rationalize the design of these catalysts, Song and Grabow performed descriptor based microkinetic model simulations combined with density functional theory (DFT) to computationally screen metal catalysts for

* Corresponding author.
E-mail address: kostas.goulas@oregonstate.edu (K.A. Goulas).

https://doi.org/10.1016/j.apcatb.2023.123329
Received 1 May 2023; Received in revised form 20 September 2023; Accepted 22 September 2023
Available online 26 September 2023
0926-3373/© 2023 Elsevier B.V. All rights reserved.

low temperature CO oxidation. The results of the model are consistent with the observed high activity of Pt:Pd alloys under standard diesel conditions (327 °C, low CO concentration). The model also simultaneously predicts poor activity at lower temperature and higher CO concentration (LTC conditions). The results of the screening indicate no single metal effectively oxidizes CO under LTC conditions. Therefore, the authors investigated alloys of transitions metals. The authors hypothesize weaker binding of π-acidic adsorbates (CO/NO) to coinage metals in alloys of these type. It was determined bimetallic alloys of Platinum Group Metals (PGMs – Pd and Pt) and coinage metals (Cu, Ag) should offer lower temperature activation for CO oxidation under LTC conditions, with NO present. [17].

The predictions of the above theoretical work have not yet been tested experimentally in the open literature; a recent patent indicates improved performance of PdCu for CO oxidation compared to PdPt. Our central hypothesis is that doping Pd nanoparticles with Cu, will result in the formation of Pd surfaces decorated with Cu. This surface Cu alleviates poisoning and competitive adsorption effects by enabling oxygen adsorption. To probe this hypothesis, a Pd on SiO_2 catalyst and 3:1 PdCu (molar ratio) on SiO_2 catalyst are prepared and compared in terms of CO oxidation activity, NO inhibition affects, surface composition, and structural properties of the catalyst nanoparticles using in situ characterization techniques. We find 3:1 PdCu has superior low temperature activity in the presence of NO, compared to Pd. Pd nanoparticles undergo a coordination number shift from a metallic phase to one representative of a Pd-O surface layer and metallic core. Conversely, the Pd in 3:1 PdCu shows no changes in coordination number. Furthermore, Cu K-edge XAS data indicates partial Cu oxidation during lightoff. Diffuse reflectance infrared spectroscopy (DRIFTS) demonstrates the formation of Pd-NO surface species during CO-NO co-oxidation over Pd, which are absent in the PdCu catalyst. Taken together, these observations show that the improved activity of PdCu catalysts compared to Pd is due to destabilization of surface-bound NO, thus preventing surface poisoning.

2. Methods

2.1. Catalyst synthesis

We synthesized a silica-supported monometallic Pd and an alloy PdCu catalyst with a 3:1 Pd:Cu atomic ratio. We used the strong electrostatic adsorption (SEA) method reported by Jiao and Regalbuto. [18] The Pd catalyst had a 4% Pd loading and the 3:1 PdCu had 2.5% Pd and 0.5% Cu by weight. For the synthesis, 5 g of silica gel (Davisil 636, Millipore Sigma) were mixed with 45 mL of deionized water (18.2 MΩ) and 4 mL of stock ammonium hydroxide solution. The palladium nitrate and copper nitrate precursor (TCI America) were dissolved in 5 mL of water, to which 4 mL of stock ammonium hydroxide solution were added. The solution of metal ammine nitrate precursors was added to silica under vigorous stirring. The mixture was stirred for 1 h and the solids were separated from the liquid by vacuum filtration. The retentate was washed with 100 mL of water and then dried under ambient air pressure at 90°C for 16 h. Portions of the dried solids were then treated for 4 h under flowing air (100 cm^3 $min^{-1}g^{-1}$) in a tubular furnace at 700°C with a heating rate of 5°C min^{-1}.

2.2. Catalyst characterization

2.2.1. Electron microscopy

Prior to electron microscopy characterization, undiluted powdered samples were reduced for 2 h at 300 °C under a flow of 4% H_2/Ar. Samples were prepared for transmission electron microscope (TEM) imaging by grinding them with a mortar and pestle, suspending the samples in ethanol and sonicating them for 15 min. They were then deposited on carbon type B 300 mesh Cu grids (Ted Pella). TEM analysis was performed on a FEI TITAN 80–200 TEM/STEM microscope. Samples were imaged at 200 kV with a typical magnification of 200 – 300 kx. The average particle diameter was determined from greater than 100 imaged particles.

2.2.2. FTIR

FTIR measurements were performed using a Thermo Nicolet iS50 FTIR spectrometer, equipped with a Harrick DRIFTS cell. A liquid nitrogen-cooled Mercury Cadmium Telluride (MCT) detector was used for data acquisition and the native OPUS software for data processing. A gas manifold with mass flow controllers was used to deliver gases (H_2, 1% NO/N_2, 10% CO/He, 20% O_2/He) to the Harrick cell and the outlet gaseous species were analyzed with a Hiden QGA mass spectrometer. We performed four probing experiments: CO temperature programmed desorption (TPD), NO TPD, in situ CO/O_2 temperature programed oxidation (TPO), and in situ CO/NO/O_2 TPO. In all experiments, 20 mg of undiluted catalyst was crushed, and loaded onto a bed of γ-Al_2O_3 within the DRIFTS cell. Before experiments catalysts were reduced in H_2 at 250 °C for 45 min (20 cm^3 min^{-1}, 60 L g^{-1} h^{-1}space velocity). The cool, post reduction catalyst is used as the background in all experiments. 10% CO (balance He) was used to saturate the surface during CO TPD. 1% NO (balance N_2) was used to saturate the surface during NO TPD. Gasses were fed at 20 cm^3 min^{-1} to the cell during TPD experiments (individually, for CO TPD, NO TPD, purging with He). Probing gases were allowed to fill the cell for 15 min and were then purged for 15 min. In TPD experiments 10 °C min^{-1} heating ramp rates were used. In oxidation experiments, the same steps were used through the reduction and background procedures. Oxidations took place with the same gases, and 20% O_2 (balance He). For CO/O_2 oxidations CO was fed at 10 cm^3 min^{-1} and O_2 at 20 cm^3 min^{-1}. For CO, NO, and O_2 oxidations, CO was fed at 7 cm^3 min^{-1}, NO at 3 cm^3 min^{-1}, and O_2 at 20 cm^3 min^{-1}. These flowrates correspond to 90 L g^{-1} h^{-1} space velocity. In oxidation experiments 5 °C min^{-1} heating ramp rates were used. FTIR spectra were recorded at 4 cm^{-1} resolution with 30 scans merged to generate one spectrum with improved signal-to-noise. For room temperature NO TPD data, a 20-point rolling average applied to smooth waviness in the spectra shown in Fig. S2C. Redhead's method was used to determine coverage by taking the integral of the area under the CO binding peak locations present in FITR spectra. [19] These peak areas were normalized to the largest individual peak in Figs. 3 and 5 below. All peaks were fit using Gaussian, Lorentzian, or Voigt fitting functions to determine the appropriate number of peaks under each spectral peak and the area under each peak. A full analysis of peak fitting is included in the SI.

2.2.3. XAS

X-ray absorption spectroscopy (XAS) data were recorded at beamline 9–3 at the Stanford Synchrotron Radiation Lightsource using a liquid nitrogen cooled double Si(220) ($\varphi = 0$ °) crystal monochromator with Rh-coated collimating and focusing mirrors for harmonic rejection. X-ray absorption near edge structure (XANES) and extended X-ray absorption fine structure (EXAFS) spectra were collected at the Cu (8979.0 eV) and (24350.0 eV) Pd K-edges in fluorescence mode using a PIPS diode. A reference spectrum of a Cu or Pd foil was collected in transmission mode simultaneously, using N_2 or Ar-filled ion chambers, respectively, for energy calibration and spectra alignment.

In all experiments, catalysts were diluted in a 1:5 ratio with MCM-41 silica (Aldrich), such that 40 mg of total material filled the polyimide tube ("Kapton", 3 mm diameter) plug flow reactor (Fig. S14). [20] At the Pd K-edge, EXAFS spectra were recorded in continuous scan mode (92 s scans/scan) for a series of temperature programmed reductions (TPRs) and oxidations (TPO) both catalysts. EXAFS spectra were acquired for the Cu K-edge also in continuous scan mode with the 3:1 PdCu catalyst during TPOs and TPRs. However, with 9 merged scans at each temperature, the signal to noise in the EXAFS region of the data is low for the Cu edge. Therefore, only the XANES region of the Cu spectrum are shown. The reduction procedure follows the same process described in the activity testing section below (20 cm^3 min^{-1}, 60 L g^{-1} h^{-1}space velocity). For oxidation, the gas flow rates were adjusted to 14 cm^3 min^{-1} for

oxygen, 1.3 cm^3 min^{-1} for CO, and 1 cm^3 min^{-1} for NO (90 L g^{-1} h^{-1}space velocity). The gas composition is the same as described FTIR section above. Operando TPO experiments used 10 °C stepwise temperature increases to ensure adequate signal-to-noise ratio in the EXAFS data (by taking either 4 or 9 scans at each temperature).

Data preprocessing and fitting were performed in the Demeter suite. [21] Cu K-edge XAS data were calibrated to 8979.0 eV by defining the edge as the location of the maximum peak in the derivative of xμ(E). Pd K-edge data was calibrated to 24350.0 eV (maximum peak in the derivative of xμ(E)). xμ(E) data were aligned using metal foil standards. During Pd edge TPOs, 4 scans were merged to achieve improved signal/noise. During Cu edge TPOs, 9 scans were merged. TPR experiments have 1 scan per temperature. Linear combination fitting (LCF) was performed on all XANES data resulting from temperature-programmed experiments using the as-prepared catalyst and the post-reduction catalyst as fitting standards. The former state is labeled as "oxidic" and the latter as "metallic". Since the Cu is alloyed in Pd, the spectra of these states will be subtly different from the spectrum of a metallic or oxidic bulk Cu. To accommodate for this, LCF fits use the scans of the "as prepared" and "reduced" catalyst for references. A justification for this choice is include in the Cu Edge LCF Fittings Standards section of the SI, which indicates the as prepared catalyst EXAFS region is dominated by Cu-O coordination, and the post reduction is dominated by Cu-Pd and Cu-Cu coordination. EXAFS fits were performed using a *k*-range of 3.5–12.5 $Å^{-1}$ and a *R*-range of 1–3 Å. Scattering paths were acquired from Materials Explorer. [22] The paths were downloaded as Pd and edited to contain a Pd-Cu path. Fits for TPOs and TPRs were performed simultaneously for all temperature intervals. The amplitude reduction factor (S_0^2) is 0.87, as determined by a fit to the Pd foil (Fig. S17). Catalytic conversion data for reactions was tracked using an online Hiden QGA mass spectrometer. All fitting parameters and fits in *R* and *k*-space are shown in the XAS section of the SI.

2.3. Catalyst activity testing

We performed multi component oxidation experiments on the two synthesized powder catalyst using a plug flow reactor which holds catalyst and allows reagent and product gases to flow to a FTIR (California Analytical Instrument 600 FTIR (SC)) gas cell which measures outlet concentrations. A gas manifold with electronic mass flow controllers is used to deliver reactant gases (H_2, N_2, 200 ppm NO in N_2, 2% O_2 in Ar, and 20% CO in He) to the reactor, a Legato 100 syringe pump is used to introduce water into the reactor and the effluent is analyzed by FTIR. In all experiments, the catalyst was diluted 1:1000 with silica gel (Davisil Grade 635 Silica gel, pore size 60 Å, 60–100 mesh) by repeated crushing and pelletizing processes, sieved to eliminate particles smaller than 106 μm, and loaded into the glass reactor directly on top of the porous frit in the reactor chamber. Since the two catalysts have different metal loadings, dispersion based on TEM measured particle size was used to load equal surface moles of each catalyst. Detailed calculations and assumptions for the surface mole estimation are located in the SI. 840 mg of diluted Pd and 1000 mg of diluted 3:1 PdCu result in 2.65 surface micromoles of catalyst loaded. A series of three trials were conducted to test the activity of Pd and 3:1 PdCu, which each consist of repeated series of TPOs, but under different gas compositions. A gas manifold with electronic mass flow controllers is used to deliver reactant gases to the reactor, and the effluent is analyzed by FTIR. The gas feed and reactor composition are shown in Table 1. Trial 1 is performed at low NO and O_2 concentration in dry conditions. Trial 2 and 3 are performed in wet conditions. Trial 2 has higher reagent concentrations (NO and O_2), and Trial 3 does not repeat the initial reduction between each TPO. There are multiple TPOs run for each trial.

The fresh (as prepared) catalyst is reduced with pure H_2 flowing at 20 cm^3 min^{-1} while being heated at 6 °C min^{-1} from room temperature (RT) to 250 °C and held for 45 min before cooling to RT. For Trial 1 and 2 this process is repeated before each TPO. A total of three TPO are run for Trial 1 and 2, and four for Trial 3. For Trial 1 TPO experiments, CO (0.5 kPa) and O_2 (1.5 kPa) are introduced with a gas hourly space velocity (GHSV) of 22,000 h^{-1}g Pd^{-1} (990 L g^{-1} h^{-1}) and 18, 400 h^{-1}g $PdCu^{-1}$ (832 L g^{-1} h^{-1}). For, Trial 2 and Trial 3 TPO experiments CO (0.5 kPa) and O_2 (15 kPa) are introduced with a gas hourly space velocity (GHSV) of 27,200 h^{-1}g Pd^{-1} (1200 L g^{-1} h^{-1}) and 23,000 h^{-1}g $PdCu^{-1}$ (1030 L g^{-1} h^{-1}).

For TPOs, the system is heated at a ramp rate of 2 °C min^{-1} from 25% to 100% CO conversion. After 100% conversion is achieved, the system is cooled to room temperature. Experiments from Trials 1 and 2 are reduced again under the typical TPR conditions and cooled to RT. The second TPO follows the same procedure as the first with the addition of NO (concentrations in Table 1). Trial 3 experimental conditions have no intermediate reduction between TPO runs, such that TPO run 2 begins immediately after cooling from TPO run 1. TPO 2 and 4 contain NO in Trial 3 experiments.

This process of heating and cooling during reduction and oxidation conditions is illustrated in Fig. S1. The purpose of this series of three reductions and oxidations is to use the average of the 1st and 3rd TPO runs to eliminate deactivation effects in the comparison of CO single oxidation with NO/CO co-oxidation. Trial 3 was performed to probe activity without intermediate reductions for comparison. A 20-point rolling average, corresponding to 5 s, was applied to conversion data to reduce noise (Fig. 2).

3. Results and discussion

3.1. Particle size and activity calculations

3.1.1. TEM

TEM showed that the average nanoparticle diameter in the supported Pd catalyst was 3 ± 0.6 nm and in the 3:1 PdCu was 3 ± 1 nm from an analysis of 100 particles. Fig. 1 displays representative images of the 3:1 PdCu catalyst. Particles in all samples appeared approximately spherical in appearance and uniform in size. The measured particle size distributions are shown in Table S1. Fig. S34 contains additional TEM images.

3.1.2. Catalytic activity

Fig. 2 shows representative light off activity curves for the CO TPO for the Pd and 3:1 PdCu catalysts from Trial 1 experiments. The Pd catalyst shows severe inhibition when NO is added to the reagent stream (Panel A, Run 2 - red). The 3:1 PdCu sample shows minimal inhibition when NO is included as a competitive reagent. Moreover, the TPO curves are less steep, indicating smaller values for the activation energy. Table 2 displays the T_{50}, the temperature at 50% conversion, for all catalysts tested. The T_{50} is often used for exothermic reactions to objectively compare the intrinsic activity before exotherms form in the reactor as a result of the CO conversion to CO_2. [23] The standard

Table 1
Feed (bottle) reagent composition, reactor composition, and reduction conditions during catalyst activity tests (TPOs).

Trial	Feed Composition				Reactor Composition				Intermediate Reduction?
	O2 (%)	CO (%)	NO (ppm)	H2O (%)	O2 (%)	CO (%)	NO (ppm)	H2O (%)	
1	2	20	200	0	1.4	0.5	50	0	Yes
2	20	20	1000	100	12	0.6	400	1.2	Yes
3	20	20	200	100	12	0.5	50	1.2	No

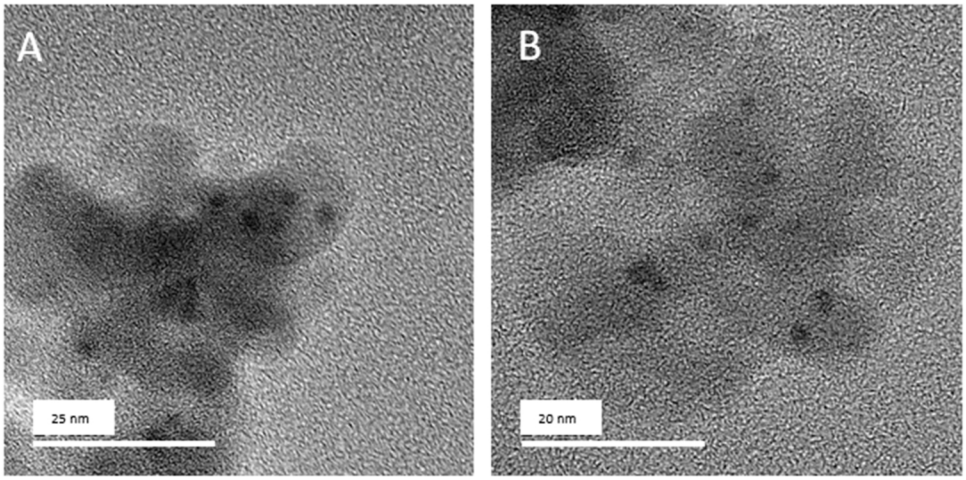

Fig. 1. TEM images from Pd (A) and 3:1 PdCu (B). Note difference in scales.

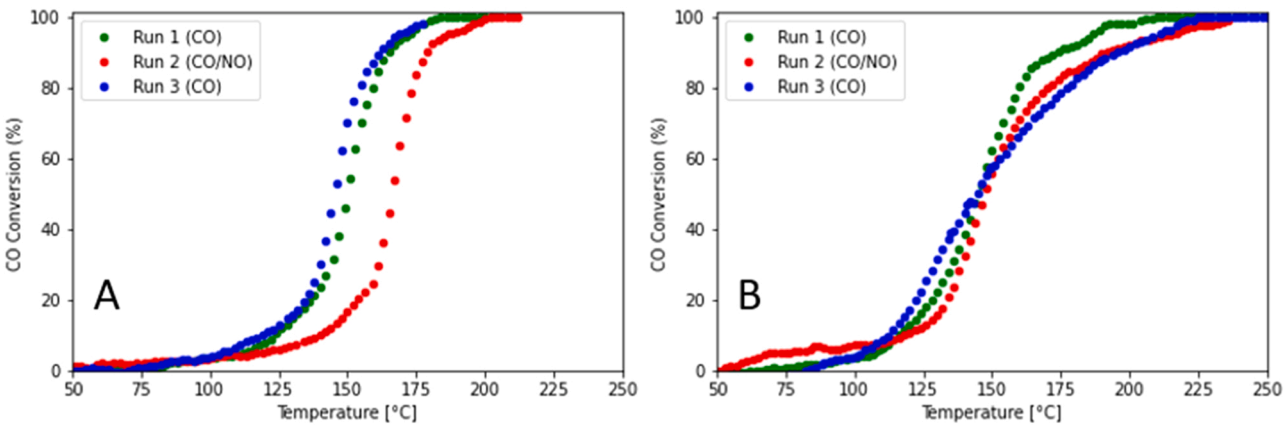

Fig. 2. Conversion versus temperature for Pd/SiO_2 (A) and 3:1 PdCu/SiO_2 (B) under Trial 1 conditions. Run 1 (green) and 3 (blue) contain only CO and O_2. Run 2 (red) contains NO. Conversion is measured as a percentage of CO via inline FTIR and temperature represents reactor temperature. Total Pressure: 101.325 kPa, O_2 partial pressure: 1.5 kPa, CO partial pressure: 0.5 kPa, 50 ppm NO when present. 2 °C min^{-1} heating rate. 22,000 h^{-1}g Pd^{-1} (990 L g^{-1} h^{-1}) and 18, 400 h^{-1}g $PdCu^{-1}$ (832 L g^{-1} h^{-1}) GHSV.

Table 2
T_{50}s values for trial 1 TPO runs for all catalyst tested and extent of inhibition when introducing NO as a competitive reductant. Total gas pressure: 101.325 kPa, O_2 partial pressure: 1.5 kPa, CO partial pressure: 0.5 kPa, 50 ppm NO when present. Space velocity: 22,000 h^{-1}g Pd^{-1} (990 L g^{-1} h^{-1}) and 18, 400 h^{-1}g $PdCu^{-1}$ (832 L g^{-1} h^{-1}). 2 °C min^{-1} heating rate.

	Pd	3:1 PdCu
T_{50} Run 1 (°C)	149	145
T_{50} Run 2 (°C)	165	146
T_{50} Run 3 (°C)	145	145
Extent of Inhibition (°C)	18	1

deviation of a typical experiment is 5.6 °C. The results in the table clearly show that the 3:1 PdCu catalyst is the better material for low temperature CO/NO co-oxidation under Trial 1 conditions. The values in Table 2 also show the extent of inhibition when NO is introduced, which is calculated as the difference between the average of Run 1 and Run 3 T_{50}s, and the run 2 T_{50}. The 3:1 PdCu shows minimal inhibition with the introduction of NO, whereas the Pd is inhibited by 18 °C. Trial 2 and 3 light off curves, and T_{50} values are shown in the Catalytic Activity section of the SI. Trial 2 and 3 data indicate water vapor is not a strong inhibitor under CO TPO conditions for either catalyst. However, the presence of water seems to reduce inhibition observed in Pd, and increases inhibition in 3:1 PdCu, when NO is introduced (Fig. S37). Trial 3 data indicate the absence of intermediate TPRs in hydrogen has little effect on T_{50}.

4. Infrared spectroscopy

The binding of CO on the catalyst surfaces was investigated by FTIR via CO TPD. Fig. 3 shows CO TPD DRIFTS spectra for Pd (A – shades of red) and 3:1 PdCu (B – shades of blue) for temperatures up to 240 °C. In both, the peak at around 2090 cm^{-1} represents CO bound to a top Pd site [24]. The atop peak shifts from 2087 to 2055 cm^{-1} for Pd and from 2090 to 2061 cm^{-1} for PdCu with increasing temperature (i.e, lower CO coverage). The slightly higher wavenumber for PdCu at ambient temperature suggests weaker CO-Pd binding in the 3:1 PdCu catalyst, compared to the pure Pd. This is in apparent disagreement with our previous theoretical work that predicts stronger binding of CO onto the Pd sites in alloy catalysts as a result of the electron density transfer from Cu to Pd during Pd-Cu alloying. [25,26] However, our previous findings investigated single CO molecules bound to flat surfaces, opposed to CO-covered multifaceted nanoparticles.

The full width at half maximum (FWHM) of the PdCu and Pd top bound peaks are 36 and 32 cm^{-1}, respectively. The PdCu and Pd bridge peaks are 70 cm^{-1} and 87 cm^{-1}, respectively, at ambient temperature (Fig. S13). The broader peak associated with the Pd sample is the result

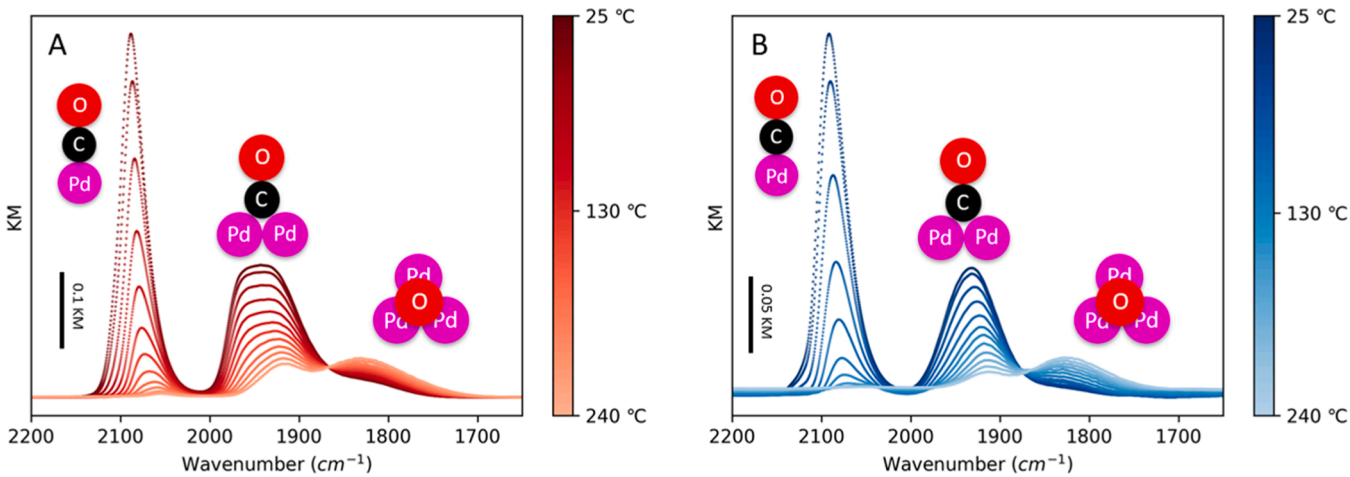

Fig. 3. CO TPD FTIR DRIFTS spectra with increasing temperature for Pd (A – shades of red) and 3:1 PdCu (B – shades of blue). Y-axis is Kubelka-Munk absorbance units, x-axis is wavenumbers (cm^{-1}). Illustrations of CO top bound to Pd and bridge bound to Pd shown next to the signals they correspond to. 10 °C min^{-1} heating rate used, 15-minute CO saturation (20 cm^3 min^{-1}), 15 min He purge (20 cm^3 min^{-1}).

of more diverse bridge bound CO species [27]. This is illustrated in Fig. S7 for Pd, and S8 for PdCu via peak fitting. This analysis confirms a single bridging site for PdCu, and two different (bridge A and B) sites in Pd. There is no evidence of surface Cu bound CO during our TPD conditions, but Cu incorporation into the Pd nanoparticles likely contributes to the lack of multiple signals, possibly by blocking Pd binding sites. The emergence of the shoulder peak at 1825 cm^{-1} represents CO on a tri-fold hollow Pd site in both spectra [24].

Top-bound and bridge-bound CO signals shift to lower wavenumbers with increasing temperature during TPD. The disappearance of the top-bound peak takes place more rapidly compared to the bridge bound peak. Additionally, the trifold peak emerges as the bridge bound peak disappears with increasing temperature. These observations have been attributed to decreasing CO coverage, in accordance with literature. [28, 29] At low temperature the Pd surface is mostly covered by CO. With increasing temperature and decreasing CO coverage, there is a shift from top bound to bridge and eventually to hollow bound adsorption due to the increased number of empty surface sites. This shift is energetically favored, as it reduces repulsive dipole-dipole interactions of top bound CO. Fig. 4 shows plots of the normalized CO coverage as a function of temperature to illustrate CO coverage modifications during TPD. With increasing temperature, there is an increase in hollow bound CO coverage with temperature for both materials, consistent with the literature. [28,29].

Fig. 5 shows in situ FTIR spectra as a function of temperature during CO oxidation. 3:1 PdCu catalyst data are displayed on the right (B), and Pd is displayed on the left (A). After light-off, CO_2 is noticeable around 2400 cm^{-1} in both spectra. Plots are shown with a full range of wavenumbers for both materials in Fig. S3. The two large peaks (2100 and 1950 cm^{-1}) displayed in the Pd spectra are CO bound to the top and bridge Pd sites, respectively. A small peak at 2180 cm^{-1} is attributed to gas phase CO. The broad, bridge-bound peak in Pd persists during TPO conditions. Further, the Pd material also shows the hollow peak at 1850 cm^{-1}, as observed in TPD. This hollow peak is absent from the PdCu material during TPO. During TPO, at temperatures above 100 °C, a new peak appears at 2130 cm^{-1} in the 3:1 PdCu sample spectrum. This peak is attributed to CO top bound to Cu [24]. This peak is absent from the PdCu during TPD, and at low temperature during TPO (Fig. S9, S12). This could suggest surface segregation of Cu as the catalyst becomes active. [24] The absence of the Cu-CO peak from the TPD and its presence in the TPO indicates that an oxidizing atmosphere is required for surface Cu segregation.

This could be attributed to an adsorbate-induced restructuring, as reported in the literature. [30] On the contrary, CO atmospheres result in Pd segregation to the surface, consistent with the binding energy trends. [17] Fig. 6 shows plots of the normalized CO coverage as a function of temperature.

The binding of NO onto Pd and 3:1 PdCu catalyst is also investigated by TPD. Fig. S2C displays spectra collected at ambient temperature during TPD for both catalysts. The peaks at 1315 cm^{-1}, 1515 cm^{-1}, and

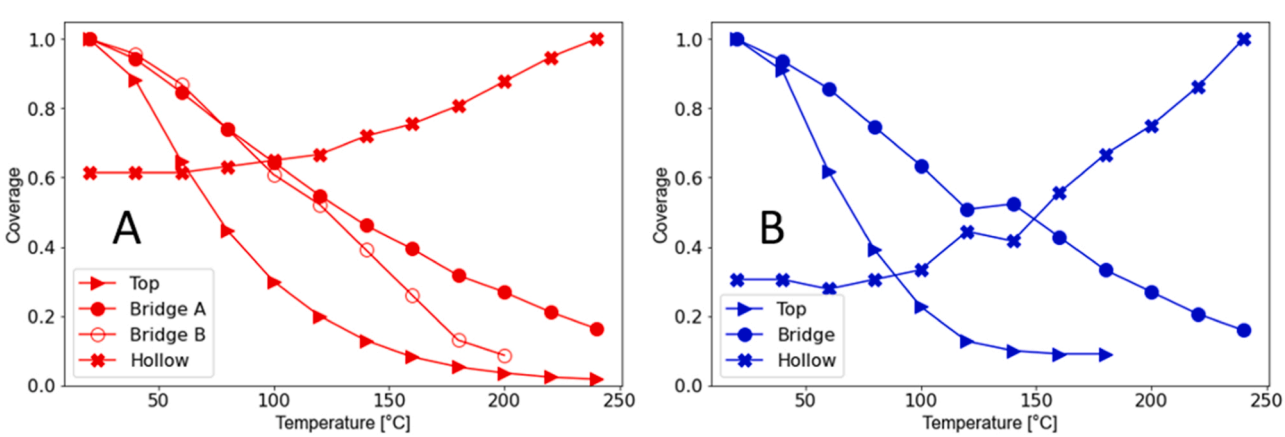

Fig. 4. Fractional coverage of different CO adsorbed species as a function of temperature for Pd (A – red) and 3:1 PdCu (B - blue) in situ DRIFTS acquired during CO TPDs. 10 °C min^{-1} heating rate, 15-minute CO saturation (20 cm^3 min^{-1}), 15 min He purge (20 cm^3 min^{-1}).

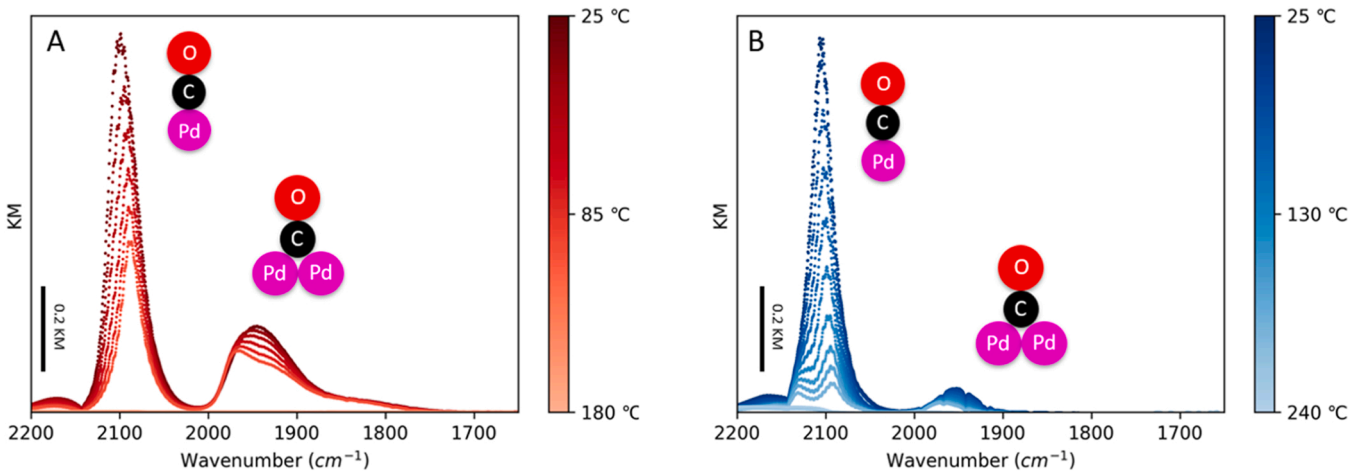

Fig. 5. In situ CO TPO FTIR DRIFTS spectra for CO oxidations (TPO). A: Pd, B: 3:1 PdCu. Y-axis is Kubelka-Munk absorbance units, x-axis is wavenumbers (cm^{-1}). Illustrations representing various binding reagents included next to corresponding peaks. Total Pressure: 101.325 kPa, O_2 partial pressure: 13.5 kPa, CO partial pressure: 3.4 kPa. 10 °C min^{-1} heating rate. 90 L g^{-1} h^{-1} space velocity.

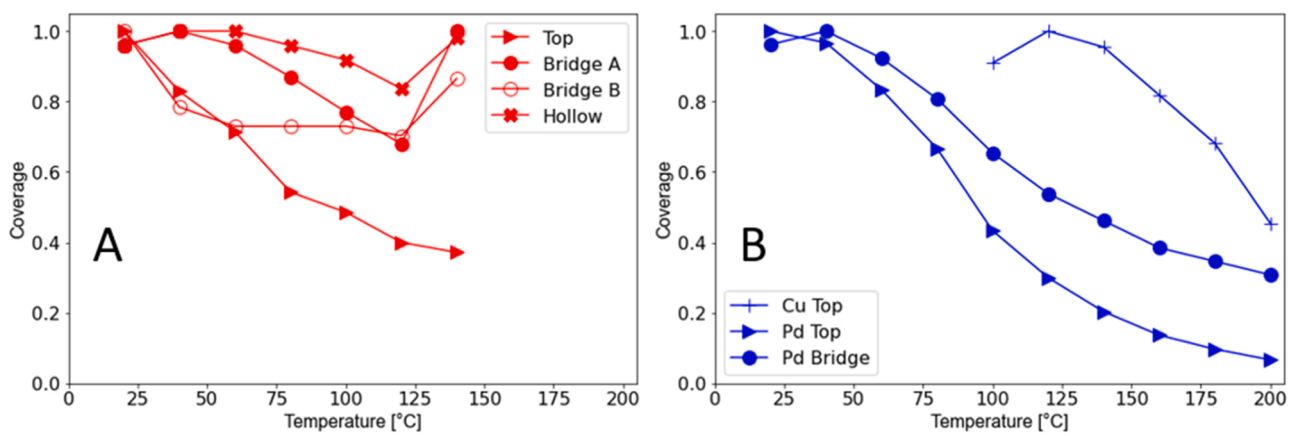

Fig. 6. Fractional coverage of different CO adsorbed species as a function of temperature for Pd (A – red) and 3:1 PdCu (B - blue) in situ DRIFTS acquired during CO oxidations. Total Pressure: 101.325 kPa, O_2 partial pressure: 13.5 kPa, CO partial pressure: 3.4 kPa. 10 °C min^{-1} heating rate. 90 L g^{-1} h^{-1}space velocity.

1535 cm^{-1} are assigned to surface nitrates [31]. The peak at 1650 cm^{-1} in 3:1 PdCu indicates formation of NO_2 on the surface. [15] The peaks at 1690 and 1780 cm^{-1} are from the formation of Pd^0-NO and Pd^{2+}-NO surface nitrosyls in the Pd material. [32,33] These Pd-NO peaks are absent in 3:1 PdCu spectra. Fig. S2 shows the spectra obtained up to 200 and 240 °C for Pd (A) and 3:1 PdCu (B), respectively, during NO TPDs.

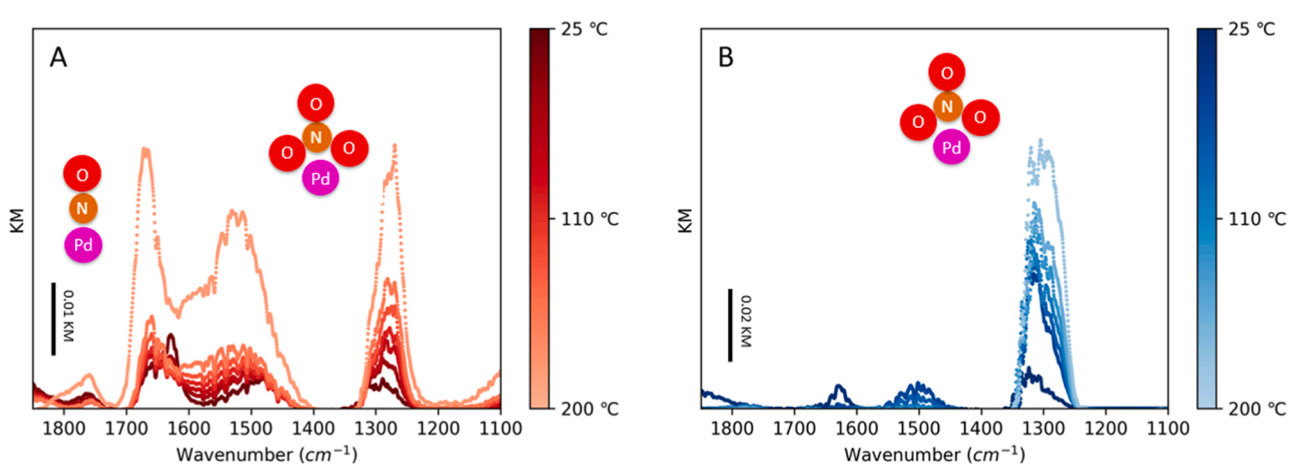

Fig. 7. In situ FTIR spectra for CO/NO oxidations. A: Pd (shades of red), B: 3:1 PdCu (shades of blue). Y-axis is Kubelka-Munk absorbance units, x-axis is wavenumbers (cm^{-1}Total Pressure: 101.325 kPa, O_2 partial pressure: 13.5 kPa, CO partial pressure: 2.4 kPa, NO partial pressure 0.1 kPa. 10 °C min^{-1} heating rate. 90 L g^{-1} h^{-1}space velocity.

Spectra during NO and CO co-oxidation are shown in Fig. 7. Full spectra (displaying CO top and bridge bound in both catalyst) are shown in Fig. S4. Fig. S5 contains a plot focused on the top bound Pd-CO peak in the 3:1 PdCu, which illustrates the emergence of Cu with temperature in the co-oxidation. Both spectra display intense nitrate peaks at 1315 cm^{-1} which increase with increasing temperature. Nitrate peaks, observed at 1515–1535 cm^{-1} are more prominent in Pd sample spectra than the 3:1 PdCu. The Pd spectra also indicate the presence of surface nitrosyl, by the Pd-NO bands at 1780 and 1690 cm^{-1}, which again are absent from the 3:1 PdCu spectra. Finally, the 3:1 PdCu spectra display a small NO_2 peak at high temperatures at 1640 cm^{-1}. [31,32].

FTIR analysis indicates Pd and 3:1 PdCu catalyst interact with CO similarly under TPD and TPO conditions. However, 3:1 PdCu contains less bridging site diversity than Pd, possibly from the presence of Cu. During CO oxidation and CO/NO oxidation, the 3:1 PdCu shows the formation of a CO top bound to Cu at high temperatures, or when the catalyst is active. This indicates that Cu segregates to the surface at high temperatures in the presence of oxidizing atmospheres. Pd spectra indicates Pd-NO formation on the surface, which is absent in 3:1 PdCu. Cu weakens the binding of NO to Pd, alleviating poisoning effects during oxidation.

5. X-ray absorption spectroscopy

5.1. Pd K-edge XAS

The Pd and the PdCu catalyst were subjected to a series of 1 TPR and 1 TPO (CO only oxidation) each while collecting Pd K edge XAS spectra. The Pd K edge XANES spectra and EXAFS spectra with the best fits are shown in Fig. S19 (Pd) and S22 (PdCu), and the modeling data are summarized in Table S8 (Pd) and S10 (PdCu) for the TPR XAS experiments. Fig. 8 shows how the coordination number for the different scattering paths changes with increasing temperature during TPR. For the Pd only sample, the Pd-O coordination number quickly drops to zero after heating starts, indicating the complete reduction of Pd at temperatures above 50 °C in H_2. The Pd in the 3:1 PdCu catalyst also reduces, with a decrease in the Pd-O coordination (at a bonding distance) to zero and increasing Pd-Pd coordination (at a bonding distance) as the sample is heated beyond 80 °C during the first reduction. At approximately 100 °C EXAFS modeling was able to fit a Pd-Cu coordination of approximately 1, indicating the formation of a PdCu alloy.

Following the reduction, the catalyst was cooled to room temperature in flowing hydrogen and then subjected to a CO oxidation (TPO 1) while acquiring Pd K-edge XAS spectra. Fig. 9 A shows the Pd K-edge XANES spectra acquired for the Pd catalyst during TPO 1. The white line region of the XANES (24360–24400 eV) of the spectra is shown in the insert in Fig. 9 A (unstacked). The change in the white line structure shows an oxidation of the Pd in the Pd catalyst. LCF analysis of the XANES spectra show that approximately 45% of the Pd was oxidized during TPO 1, Fig. S32A. Fig. 9B shows the Pd-O and Pd-Pd coordination numbers (left axis) acquired from the best fit models of the EXAFS spectra collected during TPO 1 with Fig. S31A and S9 showing the complete EXAFS results. During TPO 1 the EXAFS models show a decrease in the Pd-Pd coordination number and an increase in the Pd-O coordination number, Fig. 9B, occurring around 85 °C. The Pd-O coordination number of 1.9 ± 0.1 corresponds to approximately 47.5% of the Pd atoms being oxidized, matching the LCF results of the XANES spectra. The conversion versus temperature profile acquired during this TPO is shown in Fig. 9B (right axis), with error bars displaying the standard deviation in conversion acquired at each temperature interval. CO conversion begins to start around 55 °C with 100% conversion occurring at 80 °C. This suggest that oxidic Pd is required for CO oxidation. One point to note is that the oxidation of the Pd catalyst during the TPO occurs at a higher temperature than the change in activity itself (gap of roughly 20 °C in Fig. 9B). We believe that this could be due to two effects of the measurement. First, the sensitivity of XAS spectra to the formation of a new species requires approximately 5–10% of the absorbing atoms to change. This would mean that if the surface of the Pd was oxidized at low conversion, the XAS spectra would not be sensitive to it until a larger fraction of the particle was oxidized, causing a lag in the temperature. Secondly, the X-ray beam covered 5 mm of the catalyst bed length during the TPO. As the reaction front moves through the beam, the XAS spectra would represent an average of all the states monitors, additionally causing a lag in the temperature at which the Pd was oxidized. [9].

We observe the Pd catalyst undergoes a change in coordination from no Pd-O contribution, to a Pd-O coordination of 1.9 ± 0.1, as the catalyst heats up and becomes active for CO oxidation. Pd in bulk Pd-O would have a coordination number of 4 Pd-O. The differences observed here are due to the formation of oxidic Pd on the particle surface with a metallic core. This can be shown using particle size and dispersion, calculations are included in the SI.

The 3:1 PdCu catalyst was subjected to the same TPO 1 conditions following the reduction as the Pd catalyst. The results of the acquired XANES spectra during TPO 1 are shown in Fig. 10 A. The conversion versus temperature profile acquired during this TPO are shown in Fig. 10B (right axis), alongside the coordination number obtained from modeling the EXAFS region of this data (left axis) with Fig. S31B and Table S11 showing the details of the best fit EXAFS models. Contrary to the Pd catalyst, the local structure as determined by XAS of the 3:1 PdCu shows no changes with increasing temperature, regardless of activity suggesting that Cu may play a role in the CO oxidation.

XAS analysis indicates as prepared particles reduced to a metallic state at low temperature (<100 °C) for both Pd and PdCu under reducing conditions. The Pd in the PdCu material remains metallic regardless of CO oxidation activity whereas Pd undergoes a structural transformation to form surface oxidic Pd covering the nanoparticles as the catalyst activates for CO oxidation.

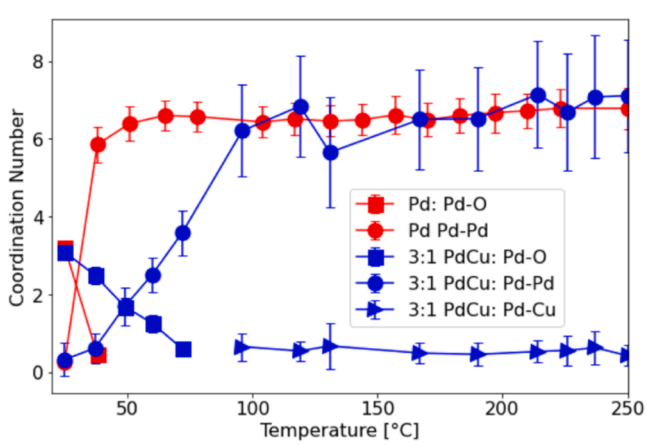

Fig. 8. Coordination number versus temperature for the in situ reduction (H_2 TPR) XAS experiments obtained from EXAFS fits of the Pd K-edge spectra. Pd catalyst data in red, 3:1 PdCu catalyst data in blue. Space velocity 60 L g^{-1} h^{-1} (pure hydrogen), heating ramp rate 6 °C min^{-1}, held at 250 °C for 45 min.

5.2. Cu K-edge XAS

Cu K-edge XAS spectra were recorded over a series of two TPRs and two TPOs for the 3:1 PdCu catalyst, similar to activity tests described above. Fig. S26 shows the XANES data acquired during TPR 1. The normalized Cu XANES spectra show a decrease in the white line intensity as the temperature is increased. Comparison of the as-prepared and reduced XANES spectra to XANES spectra of bulk Cu compounds are shown in Fig. S40. The as-prepared sample is similar to that of CuO. The lack of sharp features in the spectra suggest that the CuO exists in domains of a few nanometers. The reduce sample has an edge position

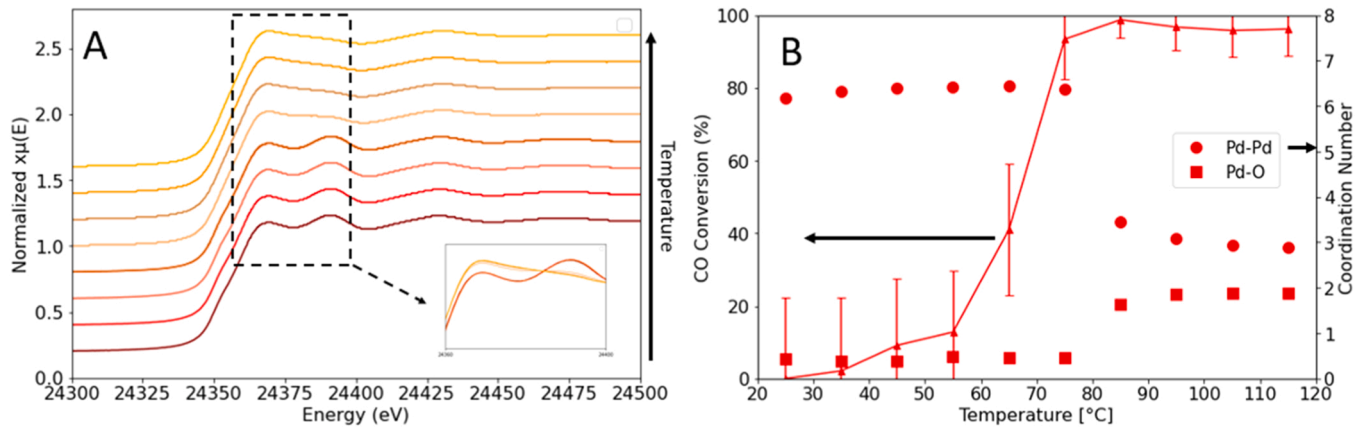

Fig. 9. Pd catalyst: (A) Pd edge XANES spectra with increasing temperature acquired during CO oxidation (insert zooms in on unstacked data between 24360 and 24400 eV to illustrate changes in white line region of spectra). (B) EXAFS coordination number modeling results for Pd-O and Pd-Pd scattering paths (left axis) during CO oxidation overlaid with the CO conversion at each point of x-ray measurement during the TPO (right axis). CO oxidation (Run 1) conditions: Total pressure: 101.325 kPa, O_2 partial pressure: 11 kPa, CO partial pressure 0.5 kPa. Heating rate of 2 °C min^{-1}, stopped every 10 °C for XANES from ambient temperature to 100% CO conversion. Space velocity 90 L g^{-1} h^{-1}.

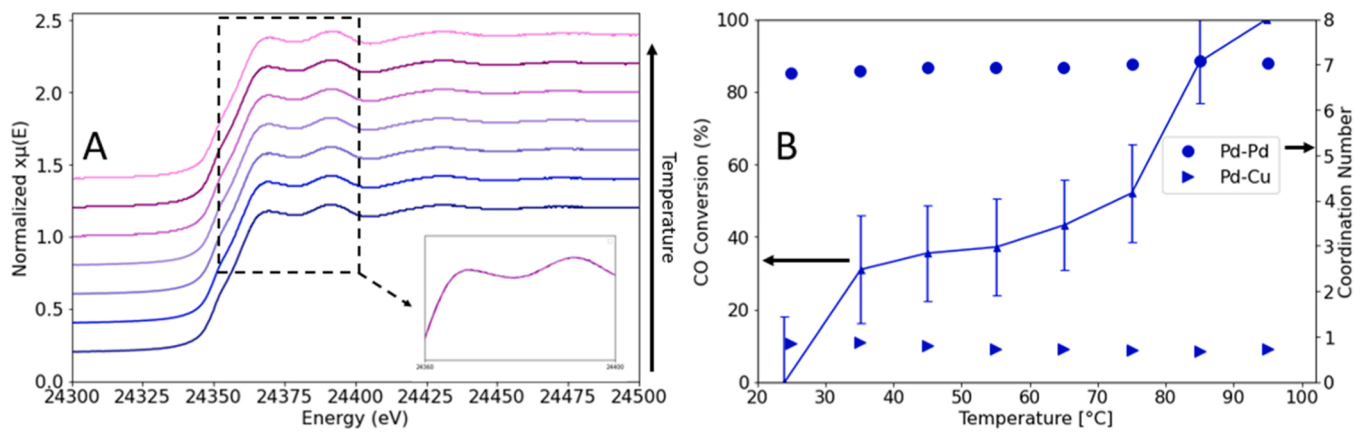

Fig. 10. 3:1 PdCu catalyst: (A) Pd edge XANES spectra with increasing temperature acquired during CO oxidation (insert zooms in on unstacked data between 24360 and 24400 eV to illustrate changes in white line region of spectra). (B) EXAFS coordination number modeling results for Pd-Cu and Pd-Pd scattering paths (left axis) during CO oxidation overlaid with the CO conversion at each point of x-ray measurement during the TPO (right axis). CO oxidation (Run 1) conditions: Total pressure: 101.325 kPa, O_2 partial pressure: 11 kPa, CO partial pressure 0.5 kPa. Heating rate of 2 °C min^{-1}, stopped every 10 °C for XANES from ambient temperature to 100% CO conversion. Space velocity 90 L g^{-1} h^{-1}.

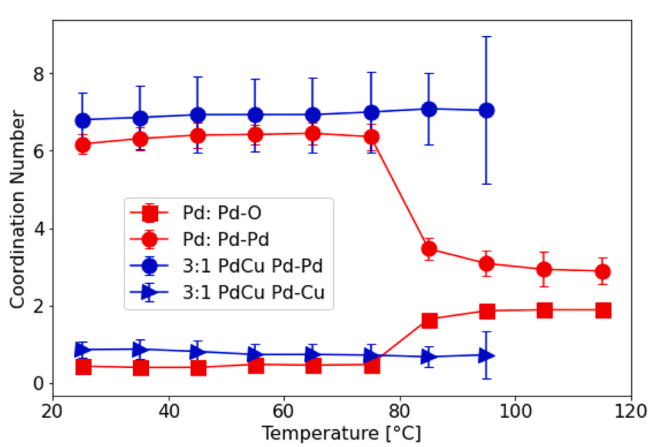

Fig. 11. Coordination number obtained via EXAFS modeling for Pd (red) and 3:1 PdCu (blue) during Run 1 CO oxidation. CO oxidation (Run 1) conditions: Total pressure: 101.325 kPa, O_2 partial pressure: 11 kPa, CO partial pressure 0.5 kPa. Heating rate of 2 °C min^{-1}, stopped every 10 °C for x-ray scans from ambient temperature to 100% CO conversion. Space velocity 90 L g^{-1} h^{-1}.

and white line shape matching that of Cu metal, however the lack of the second peak in the white line suggests that the structure is not exactly that of metallic Cu. Best fit EXAFS models of the as prepared and reduced states, Figs. S41-S42 and Table S14, show that the as prepared sample contains a Cu-O coordination (at a bonding distance) of 4.2 ± 0.4 indicating a CuO-like structure whereas the reduced state contained Cu-Cu and Cu-Pd coordination. The detection of a PdCu alloy would account for a distortion in the Cu XANES spectrum due to the influence of Pd neighbors. A model was attempted to account for incomplete reduction of the Cu, Fig. S43 and Table S15, but the model did not make good chemical sense and was rejected. Based upon the EXAFS models from the Pd and Cu XAS spectra, the as-prepared sample consisted of oxidic nanoparticles that upon reduction form PdCu bimetallic particles.

With the as-prepared representing an oxidic Cu nanoparticle species and the reduced sample representing a bimetallic PdCu nanoparticle, their respective XANES spectra were used as standards for LCF analysis of the transient Cu XANES spectra during the TPRs and TPOs. Additional details and discussion of the speciation analysis can be found in Cu Edge LCF Fittings Standards section of the SI.

LCF fits show the Cu transforming from an oxidized to a reduced species at low temperature (<100 °C) during the first reduction,

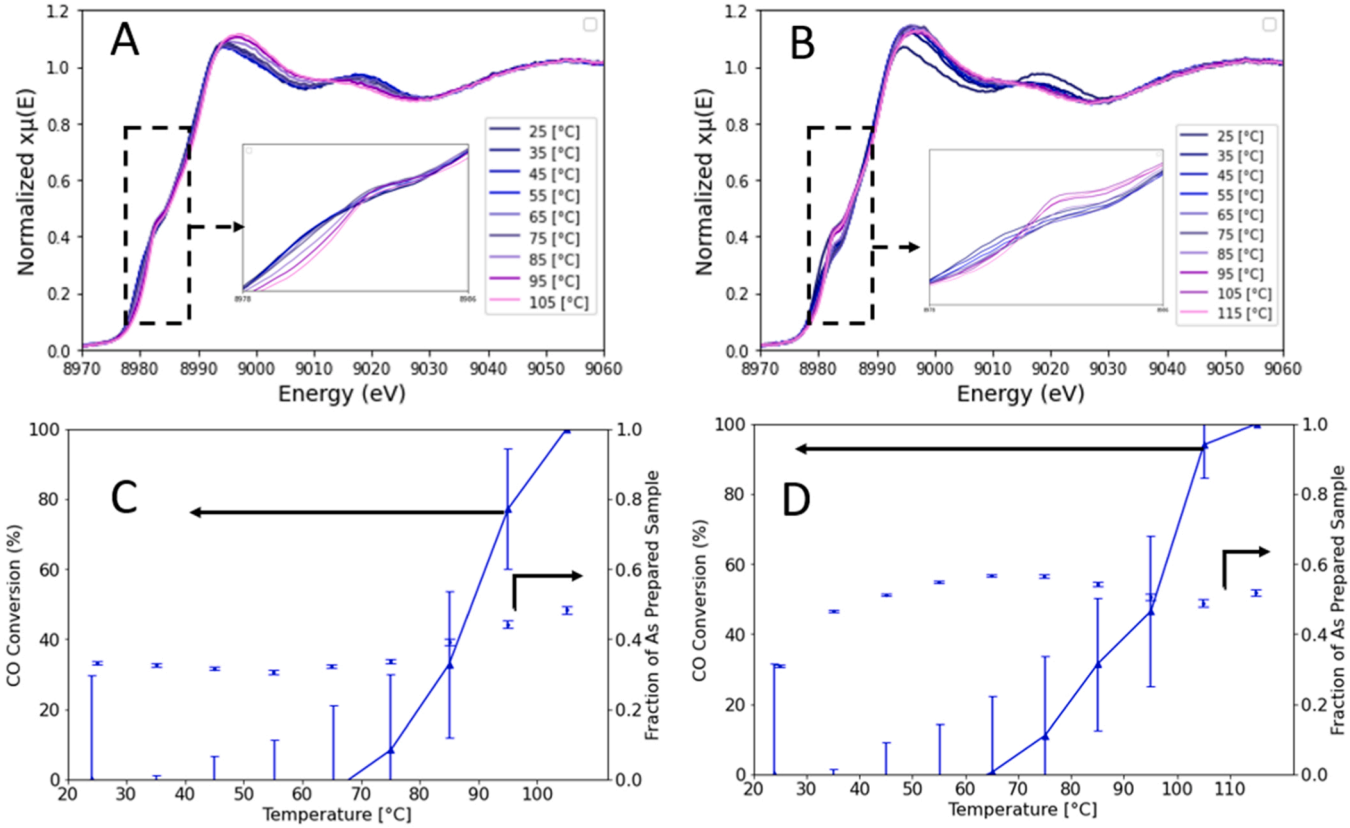

Fig. 12. Cu Edge XAS Data acquired during in situ CO oxidation (TPO) for 3:1 PdCu. XANES data: (A) TPO 1, (B) TPO 2 (CO/NO oxidation). Inserts in (A) and (B) zoom in on the pre-edge region of the spectra. Linear Combination Fitting and Conversion: (C) TPO 1, (D) TPO 2. In LCF data, markers represent the fraction of the As Prepared Catalyst Standard. Conversion: (C) shows CO conversion as a function of temperature acquired during TPO 1 while scanning the Cu edge. (D) shows CO conversion during TPO 2 (when NO is present). Error bars represent the standard deviation in conversion at each temperature. Oxidizing Conditions: Total pressure: 101.325 kPa, O_2 partial pressure: 11 kPa, CO partial pressure 0.5 kPa. Heating rate of 2 °C min^{-1}, stopped every 10 °C for x-ray scans from ambient temperature to 100% CO conversion. Space velocity 90 L g^{-1} h^{-1}.

Fig. S26. Fig. 12 A shows the Cu K-edge XANES spectra collected during TPO 1 (CO oxidation) in the PdCu catalyst. As temperature increases and the catalyst activates for CO oxidation, there is a shift in edge position, defined by the first maximum of the first derivative of the XANES spectra, and an increase in the white line intensity coupled with a shift of this peak to higher energy. Fig. 12 C displaying the conversion versus temperature and LCF XANES results. The increase in the Cu oxidation determined by LCF occurs around 85 °C trailing behind the increase in CO oxidation activity. Following reduction, our fitting standard fits indicate the Cu is fully reduced (Cu Edge LCF Fittings Standards). At the final scan in TPO 1, we see a near 40% oxidation towards the as prepared fitting standard from this reduced state. The oxidation of the Cu but not Pd in the PdCu sample, observed by XANES and EXAFS analysis, suggests that Cu is mobile in the particle and forms an oxidic species on the surface of the nanoparticle preventing the oxidation of the Pd.

Following TPO 1, the catalyst was re-reduced in hydrogen during TPR 2 (Fig. S28). The data indicate little changes in white line position or intensity from the first measurement to the last during TPR 2 (Fig. S28 LCF fits). As the hydrogen was started prior to date collection, this indicates the Cu is reduced rapidly at room temperature. Finally, the catalyst was subjected to TPO 2 (CO and NO Oxidation) following TPR 2. TPO 2 also shows a oxidation of the Cu species as a function of temperature as the catalyst activates. However, oxidation of the Cu and catalyst activation start to occur at a lower temperature (35 °C in Fig. 12D) compared to that TPO 1.

The Cu edge spectra display reversible shifts from reduced Cu (during TPR) to oxidized Cu (during TPO) through the two TPR-TPO cycles. When NO is present, activation occurs at a lower temperature than when only CO is present, facilitating the oxidation of Cu.

6. Conclusions

Pd and 3:1 PdCu catalyst are highly active for CO oxidation. Pd CO oxidation activity is inhibited in the presence of NO, while 3:1 PdCu is not at low NO concentrations. This is attributed to the formation of surface nitrosyls under NO saturation and oxidizing conditions on Pd. Conversely, the Cu-containing sample is not observed to form any surface nitrosyls by FTIR suggesting that Cu incorporation into the Pd particles reduces NO adsorption onto Pd.

FTIR analysis during oxidations indicates Cu becomes available for CO binding at elevated temperatures, before complete CO conversion is achieved. This could indicate a Cu surface migration, or desorption of oxygen from Cu at high temperature. Cu edge XAS analysis during oxidations indicates that Cu oxidizes as the catalyst becomes active for CO oxidation. This apparent oxidation combined with the emergence of the peak at high temperatures in FTIR suggest Cu migrates to the surface, and becomes available for oxygen binding. Further, we observe during Pd edge XAS analysis during oxidation, the Pd material undergoes change to form a surface oxide layer with increasing temperature. However, there is no change in Pd-Pd or Pd-Cu coordination number in the 3:1 PdCu with increasing temperature during oxidation. This further confirms that Cu indeed interacts with oxygen on the surface, preventing formation of a Pd-O layer with activation. Further XAS work with the Cu edge, specifically to model the EXAFS region during TPO, could help in understanding the role of surface Cu and oxygen.

The incorporation of Cu into Pd nanoparticles could help improve

the function of DOCs at low temperature and in the presence of competitive reagents, which will enable the clean use of highly efficient LTC diesel vehicles. Further work is required to test the durability of the catalyst under real diesel exhaust conditions, and in the presence of poisons such as sulfur, to confirm the applicability of the material as DOC component.

CRediT authorship contribution statement

SK: Investigation, Writing - Original Draft, Formal Analysis, Visualization, Funding acquisition. **SS:** Investigation. **ASH:** Resources, Writing - Review & Editing, Formal Analysis, Methodology, Project administration. **SRB:** Conceptualization, Resources, Writing - Review & Editing, Supervision, Project administration, Funding acquisition. **KAG:** Conceptualization, Resources, Writing - Review & Editing, Supervision, Project administration, Funding acquisition.

Declaration of Competing Interest

The authors declare the following financial interests/personal relationships which may be considered as potential competing interests: Stephen Kristy reports financial support was provided by US Department of Energy. Konstantinos A. Goulas has patent #US20230074054A1 pending to University of Houston, Oregon State University.

Data availability

Data will be made available on request.

Acknowledgements

S.K. was supported by the DOE BES, Office of Workforce Development for Teachers and Scientists, Office of Science Graduate Student Research (SCGSR) program, which is administered by the Oak Ridge Institute for Science and Education for the DOE under contract number DE-SC0014664. This research used resources of the Stanford Synchrotron Radiation Lightsource. Use of the Stanford Synchrotron Radiation Lightsource, SLAC National Accelerator Laboratory, is supported by the U.S. Department of Energy, Office of Science, Office of Basic Energy Sciences under Contract No. DE-AC02-76SF00515. Co-ACCESS is supported by the U.S. Department of Energy, Office of Basic Energy Sciences, Chemical Sciences, Geosciences and Biosciences Division.

Appendix A. Supporting information

Supplementary data associated with this article can be found in the online version at doi:10.1016/j.apcatb.2023.123329.

References

[1] T.J. Wallington, C.K. Lambert, W.C. Ruona, Diesel vehicles and sustainable mobility in the U.S, Energy Policy 54 (2013) 47–53, https://doi.org/10.1016/j.enpol.2011.11.068.
[2] F. Martinovic, L. Castoldi, F.A. Deorsola, Aftertreatment technologies for diesel engines: an overview of the combined systems, Catalysts 11 (6) (2021) 653, https://doi.org/10.3390/catal11060653.
[3] P. Crosignani, A. Nanni, N. Pepe, C. Pozzi, C. Silibello, A. Poggio, M. Conte, The effect of non-compliance of diesel vehicle emissions with euro limits on mortality in the city of milan, Atmosphere 12 (3) (2021) 342, https://doi.org/10.3390/atmos12030342.
[4] H. Sharma, A. Mhadeshwar, A detailed microkinetic model for diesel engine emissions oxidation on platinum based diesel oxidation catalysts (DOC), Appl. Catal. B: Environ. 127 (2012) 190–204, https://doi.org/10.1016/j.apcatb.2012.08.021.
[5] M. Khosravi, A. Abedi, R.E. Hayes, W.S. Epling, M. Votsmeier, Kinetic modelling of Pt and Pt: Pd Diesel Oxidation Catalysts, Appl. Catal. B: Environ. 154–155 (2014) 16–26, https://doi.org/10.1016/j.apcatb.2014.02.001.
[6] J. Lee, J.R. Theis, E.A. Kyriakidou, Vehicle emissions trapping materials: successes, challenges, and the path forward, Appl. Catal. B: Environ. 243 (2019) 397–414, https://doi.org/10.1016/j.apcatb.2018.10.069.
[7] V.Y. Prikhodko, S.J. Curran, J.E. Parks, R.M. Wagner, Effectiveness of diesel oxidation catalyst in reducing HC and CO emissions from reactivity controlled compression ignition, SAE Int. J. Fuels Lubr. 6 (2) (2013) 329–335.
[8] J.E. Etheridge, T.C. Watling, A.J. Izzard, M.A.J. Paterson, The effect of Pt:Pd ratio on light-duty diesel oxidation catalyst performance: an experimental and modelling study, SAE Int. J. Engines 8 (3) (2015) 1283–1299, https://doi.org/10.4271/2015-01-1053.
[9] M.J. Hazlett, W.S. Epling, Spatially resolving CO and C3H6 oxidation reactions in a Pt/Al2O3 Model oxidation catalyst, Catal. Today 267 (2016) 157–166, https://doi.org/10.1016/j.cattod.2015.11.033.
[10] C. Meephoka, C. Chaisuk, P. Samparnpiboon, P. Praserthdam, Effect of phase composition between Nano γ- and χ-Al2O3 on Pt/Al2O3 catalyst in CO oxidation, Catal. Commun. 9 (4) (2008) 546–550, https://doi.org/10.1016/j.catcom.2007.04.016.
[11] A.D. Allian, K. Takanabe, K.L. Fujdala, X. Hao, T.J. Truex, J. Cai, C. Buda, M. Neurock, E. Iglesia, Chemisorption of CO and mechanism of CO oxidation on supported platinum nanoclusters, J. Am. Chem. Soc. 133 (12) (2011) 4498–4517, https://doi.org/10.1021/ja110073u.
[12] K.G. Rappé, C. DiMaggio, J.A. Pihl, J.R. Theis, S.H. Oh, G.B. Fisher, J. Parks, V. G. Easterling, M. Yang, M.L. Stewart, K.C. Howden, Aftertreatment protocols for catalyst characterization and performance evaluation: low-temperature oxidation, storage, three-way, and NH3-SCR catalyst test protocols, Emiss. Control Sci. Technol. 5 (2) (2019) 183–214, https://doi.org/10.1007/s40825-019-00120-7.
[13] P.H. Ho, D. Yao, D. Creaser, L. Olsson, Advantages of high-siliceous zeolites in the reactivity and stability of diesel oxidation catalysts, ACS Eng. Au 2 (3) (2022) 219–235, https://doi.org/10.1021/acsengineeringau.1c00035.
[14] T.F. Garetto, E. Rincón, C.R. Apesteguía, Deep oxidation of propane on Pt-supported catalysts: drastic turnover rate enhancement using zeolite supports, Appl. Catal. B: Environ. 48 (3) (2004) 167–174, https://doi.org/10.1016/j.apcatb.2003.10.004.
[15] T. Visser, T.A. Nijhuis, A.M.J. van der Eerden, K. Jenken, Y. Ji, W. Bras, S. Nikitenko, Y. Ikeda, M. Lepage, B.M. Weckhuysen, Promotion effects in the oxidation of CO over zeolite-supported Pt nanoparticles, J. Phys. Chem. B 109 (9) (2005) 3822–3831, https://doi.org/10.1021/jp044767f.
[16] T. Franken, E. Vieweger, A. Klimera, M. Hug, A. Heel, Sulphur tolerant diesel oxidation catalysts by noble metal alloying, Catal. Commun. 129 (2019), 105732, https://doi.org/10.1016/j.catcom.2019.105732.
[17] Y. Song, L.C. Grabow, Activity trends for catalytic CO and NO Co-oxidation at low temperature diesel emission conditions, Ind. Eng. Chem. Res. (2018), acs.iecr.8b01905, https://doi.org/10.1021/acs.iecr.8b01905.
[18] L. Jiao, J.R. Regalbuto, The synthesis of highly dispersed noble and base metals on silica via strong electrostatic adsorption: I. amorphous silica, J. Catal. 260 (2) (2008) 329–341, https://doi.org/10.1016/j.jcat.2008.09.022.
[19] R.I. Masel, Principles of Adsorption and Reaction on Solid Surfaces, John Wiley & Sons,, 1996.
[20] A.S. Hoffman, J.A. Singh, S.F. Bent, S.R. Bare, In situ observation of phase changes of a silica-supported cobalt catalyst for the fischer–tropsch process by the development of a synchrotron-compatible in situ/operando powder X-ray diffraction cell, J. Synchrotron Rad. 25 (6) (2018) 1673–1682, https://doi.org/10.1107/S1600577518013942.
[21] B. Ravel, M. Newville, Athena, artemis, hephaestus: data analysis for X-ray absorption spectroscopy using IFEFFIT, J. Synchrotron Rad. 12 (4) (2005) 537–541, https://doi.org/10.1107/S0909049505012719.
[22] Materials Project - Materials Explorer. Materials Project. ⟨https://materialsproject.org/materials⟩ (accessed 2023–04-04).
[23] S.M. Al-Adwani, J. Soares, W.S. Epling, Evaluating the effects of precious metal distribution along a monolith-supported catalyst for CO oxidation, Ind. Eng. Chem. Res. 51 (19) (2012) 6672–6679, https://doi.org/10.1021/ie202969u.
[24] M.R. Ball, K.R. Rivera-Dones, E.B. Gilcher, S.F. Ausman, C.W. Hullfish, E.A. Lebrón, J.A. Dumesic, AgPd and CuPd catalysts for selective hydrogenation of acetylene, ACS Catal. 10 (15) (2020) 8567–8581, https://doi.org/10.1021/acscatal.0c01536.
[25] T. Bathena, T. Phung, S.R. Svadlenak, Y. Liu, L.C. Grabow, K.A. Goulas, Oxygenate reactions over PdCu and PdAg catalysts: distinguishing electronic and geometric effects on reactivity and selectivity, ACS Catal. 12 (10) (2022) 5766–5775, https://doi.org/10.1021/acscatal.2c00561.
[26] A. Goulas, K, Y. Song, R. Johnson, G, P. Chen, J, A. Gokhale, A, C. Grabow, L, F. Dean Toste, Selectivity tuning over monometallic and bimetallic dehydrogenation catalysts: effects of support and particle size, Catal. Sci. Technol. 8 (1) (2018) 314–327, https://doi.org/10.1039/C7CY01306J.
[27] A.S. Hoffman, C.-Y. Fang, B.C. Gates, Homogeneity of surface sites in supported single-site metal catalysts: assessment with band widths of metal carbonyl infrared spectra, J. Phys. Chem. Lett. 7 (19) (2016) 3854–3860, https://doi.org/10.1021/acs.jpclett.6b01825.
[28] D.R. Rainer, M. -C. Wu, D.I. Mahon, D.W. Goodman, Adsorption of CO on Pd/Al2O3/Ta(110) model catalysts, J. Vac. Sci. Technol. A Vac. Surf. Films 14 (3) (1998) 1184, https://doi.org/10.1116/1.580263.
[29] W. Daniell, H. Landes, N.E. Fouad, H. Knözinger, Influence of pretreatment atmosphere on the nature of silica-supported Pd generated via decomposition of Pd (Acac)2: an FTIR spectroscopic study of adsorbed CO, J. Mol. Catal. A: Chem. 178 (1–2) (2002) 211–218, https://doi.org/10.1016/S1381-1169(01)00323-5.
[30] F. Tao, M.E. Grass, Y. Zhang, D.R. Butcher, J.R. Renzas, Z. Liu, J.Y. Chung, B. S. Mun, M. Salmeron, G.A. Somorjai, Reaction-driven restructuring of Rh-Pd and Pt-Pd core-shell nanoparticles, Science 322 (5903) (2008) 932–934, https://doi.org/10.1126/science.1164170.

[31] I. Friberg, A. Wang, L. Olsson, Hydrothermal aging of Pd/LTA monolithic catalyst for complete CH4 oxidation, Catalysts 10 (5) (2020) 517, https://doi.org/10.3390/catal10050517.

[32] Karinshak, K.A. Nitrogen Oxide Uptake and Desorption on Pd/ZSM-5 and Pd/Fe/ZSM-5. Thesis, 2017. https://uh-ir.tdl.org/handle/10657/4770 (accessed 2023–01-06).

[33] T. Baidya, P. Bera, B.D. Mukri, S.K. Parida, O. Kröcher, M. Elsener, M.S. Hegde, DRIFTS studies on CO and NO adsorption and NO+CO reaction over Pd2+-substituted CeO2 and Ce0.75Sn0.25O2 catalysts, J. Catal. 303 (2013) 117–129, https://doi.org/10.1016/j.jcat.2013.03.020.